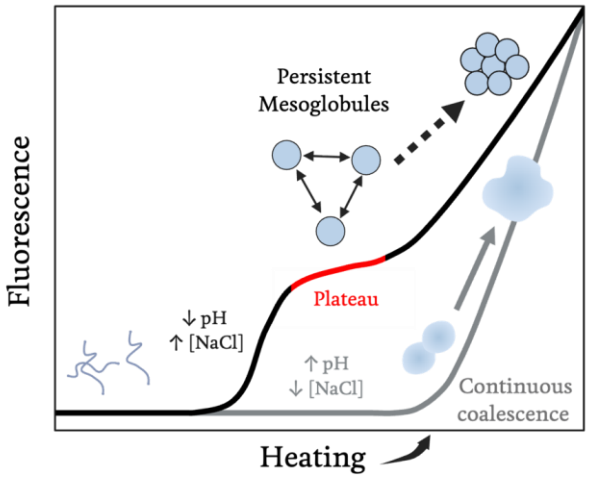
Phase-Separation Pathway Selection in PNIPAM through End-Group Ionisation and NaCl Salting-Out

Yuhang Zhang[1], Tianlai Xia[2], Qin Jin[1], Thieme T. Schmidt[1], Rachel K. O'Reilly[2], Ulrich F. Keyser[3,*], and Jeremy J. Baumberg[1,*]

[1] NanoPhotonics Centre, Cavendish Laboratory, Department of Physics, University of Cambridge, Cambridge CB3 0HE, United Kingdom

[2] School of Chemistry, University of Birmingham, Edgbaston, Birmingham B15 2TT, United Kingdom

[3] Cavendish Laboratory, Department of Physics, University of Cambridge, Cambridge CB3 0HE, United Kingdom



*Corresponding Authors

Ulrich F. Keyser: ufk20@cam.ac.uk

Jeremy J. Baumberg: jjb12@cam.ac.uk

Abstract

Nile Red fluorescence revealed three distinct phase-separation pathways in heterotelechelic HS–PNIPAM–COOH: multistage, monotonic, and suppressed transitions. Aqueous HS–PNIPAM–COOH ($M_n \approx 6$ kDa) was investigated over pH 3–10 and at NaCl concentrations from 0 to 1.0 M using fluorescence, turbidimetry, dynamic light scattering, and temperature-controlled single-particle tracking. Multistage transitions, comprising an initial fluorescence rise, an intermediate plateau, and a second rise, occurred under weakly ionised, high-salt conditions. Intermediate conditions produced a monotonic fluorescence increase, whereas strongly ionised, weakly screened conditions suppressed phase separation. The multistage sample, citrate containing 1.0 M NaCl, formed stable, micrometre-scale PNIPAM-rich droplets close to their final size that showed no further growth across the fluorescence plateau despite increasing turbidity. Growth resumed only above the plateau. By contrast, the representative monotonic samples (citrate without added NaCl and borate containing 1.0 M NaCl) showed continuous droplet growth during the temperature holds. During cooling, multistage droplets remained nearly unchanged in size on cooling from 60 to 40 °C before undergoing delayed, rapid, collective dissolution at lower temperature, whereas monotonic droplets shrank progressively before later rapid dissolution. These results show that pH and NaCl concentration control both the phase-separation pathway and mesoglobule persistence, producing different high-temperature states that rehydrate differently on cooling.

1. Introduction

The thermoresponsive coil-to-globule transition of poly(*N*-isopropylacrylamide) (PNIPAM) and its subsequent phase separation are central to responsive soft-material design.[1] On heating through its lower critical solution temperature (LCST) in water, PNIPAM chains partially dehydrate and collapse from hydrated coils into compact globules.[2] At sufficient concentration, these globules associate into larger clusters that may grow continuously or persist as relatively monodisperse, colloidally stable mesoglobules.[3–5] Controlling mesoglobule formation and persistence is important for applications ranging from triggered drug release, where colloidal stability near physiological temperature is desirable,[6] to aqueous 3D printing, where rapid phase separation and precipitation are required.[7]

Mesoglobule stability depends strongly on interfacial dynamics. Nonradiative energy transfer and fluorescence-depolarisation measurements showed that PNIPAM mesoglobules formed just above the demixing temperature are initially fluid-like and capable of merging but become rigid and non-merging within a further 6 °C of heating.[8] Small-angle neutron scattering (SANS) measurements performed under pressure show that, under strongly dehydrating conditions, collapsed PNIPAM globules initially grow by diffusion-limited coalescence into fractal-like clusters but then develop a dense polymer-rich shell at the mesoglobule surface that impedes chain interpenetration and arrests further coalescence.[9–11] Under less dehydrating conditions, no such shell forms, and mesoglobules instead grow by unhindered diffusion-limited coalescence. Pressure-jump experiments also identified two dissolution modes: under weak driving forces, mesoglobules shrank primarily by release of individual chains from the surface, whereas under stronger osmotic driving forces water swelled the mesoglobule interior first, loosening chain association and accelerating disintegration.[12] Although these studies used pressure rather than temperature as the control variable, they suggest that mesoglobule formation,

arrest, and dissolution are governed by how rapidly dehydration proceeds relative to the time-scale of interfacial relaxation and chain rearrangement.

Here we explore whether the same dynamics can be accessed by tuning solution variables. Previous work shows that NaCl can both screen electrostatic repulsion and enhance PNIPAM dehydration. NMR measurements indicate that NaCl lowers the energetic cost of hydrophobic contact formation during early chain collapse,[13] and Zhang et al. showed that NaCl depresses the LCST primarily by increasing the surface-tension penalty around hydrophobically hydrated moieties.[14] Increasing the NaCl concentration may therefore accelerate dehydration and favour an arrested mesoglobule state. End-group ionisation provides another control, particularly for low-molecular-weight PNIPAM, where the termini contribute substantially to the overall polymer character.[15–17] Carboxyl-terminated PNIPAM stars, for example, remain unimeric above the LCST when their termini are strongly deprotonated but aggregate readily at lower pH or after salt addition.[18] Ionisation also alters local hydration: carboxylates are strongly hydrated,[19] and acrylic-acid-containing PNIPAM copolymers show increased hydration and electrostatic stabilisation under deprotonated conditions.[20,21] Thus, pH and NaCl may jointly control electrostatic repulsion, terminal-group hydration, and the rate of interfacial dehydration.

Resolving this interplay requires measurements spanning several structural scales. Nile Red reports changes in the local polymer-rich microenvironment because its fluorescence is weak in aqueous PNIPAM solutions below the LCST but rises sharply above the transition as the dye partitions into hydrophobic polymer-rich domains.[22] Turbidimetry detects larger, optically distinct structures; dynamic light scattering (DLS) reports ensemble relaxation dynamics; and single-particle tracking directly resolves droplet-scale growth and dissolution. Combining these probes allows local dehydration to be related to the emergence, evolution, and persistence of mesoscopic PNIPAM-rich assemblies.

In this work, heterotelechelic HS–PNIPAM–COOH ($M_n \approx 6$ kDa) serves as a model system with two ionisable termini: the carboxyl group deprotonates near pH 4–5,[23] whereas the aliphatic thiol deprotonates near pH 9–11.[24] By varying the pH from 3 to 10 and the NaCl concentration from 0 to 1.0 M over repeated thermal cycles, we identify three distinct phase-separation behaviours: (i) multistage transitions with long-lived mesoglobule intermediates, (ii) monotonic transitions, and (iii) effective suppression of interchain association. We show that rapid heating into the fluorescence-plateau region generates micrometre-scale mesoglobules close to their final size that remain stable throughout the temperature hold. The fluorescence profile therefore provides an operational map for selecting conditions that produce either stable mesoglobule populations or continuously growing clusters, offering a practical route to control cluster size and kinetic stability through solution pH, NaCl concentration, and temperature.

2. Methods

2.1 Materials and sample preparation

Heterotelechelic HS–PNIPAM–COOH (M_n = 6 kDa; reported M_w/M_n = 1.2; Sigma-Aldrich) was dissolved in water at 1 mM. The measured dispersity was M_w/M_n = 1.12 (Supporting Information, Section S1). Before use, the polymer was treated with 10 mM tris(2-carboxyethyl)phosphine (TCEP; Invitrogen) at pH 7.4 and 25 °C for 30 min to reduce disulfides formed during storage and measurement.[25,26] TCEP itself did not measurably change the phase transition of a thiol-free PNIPAM–COOH control across repeated thermal cycles, whereas omitting TCEP allowed disulfide formation in HS–PNIPAM–COOH and altered its response (Section S2 and Figure S6). Purification of the as-received polymer by precipitation did not change the measured transition temperatures, and the concentration-dependent cloud point of the polymer in pure water is reported in Section S1.

For each measurement, 25 µL of reduced polymer stock was added to 1 mL of 10 mM citrate (J61391.AK; pH 3.0), Tris (J60636.K2; pH 7.4), or borate (J62154.AK; pH 10.0) buffer

(Thermo Scientific); pH values were adjusted and measured at 25 °C. NaCl was added to final concentrations of 0, 0.1, 0.5, or 1.0 M. A 10 mM MOPS buffer (J61843.AP) was also included because its pK_a has a smaller temperature coefficient than that of Tris ($\Delta pK_a/\Delta T \approx -0.011$ °C^{-1} compared with −0.028 °C^{-1}); the MOPS measurements and the estimated pH–temperature profiles of all buffers are given in Section S3. Samples and polymer-free blanks were prepared in ultrapure water and filtered through 0.22 µm Millex PES filters. Buffer concentrations were limited to 10 mM to reduce ionic-strength and specific-ion effects.[27,28] For the extended pH series at 1.0 M NaCl, samples were prepared similarly at pH 5.5–7.0 in 10 mM MES buffer (J61587.AP) and at pH 4.5 in 10 mM citrate buffer (Section S6).

2.2 Nile Red fluorescence

Nile Red (Sigma-Aldrich) was prepared in DMSO at 1 mg mL^{-1} and added to each sample at 7.8 µM; dye-concentration controls are provided in Section S4. Fluorescence was recorded in Hellma cuvettes using a Cary Eclipse fluorometer (λ_{ex} = 543 nm; λ_{em} = 650 nm). Samples underwent four heating–cooling cycles from 10 to 60 °C at 1 °C min^{-1}. Signals from matched polymer-free blanks were subtracted (Figure S8a).

2.3 Turbidimetry

Turbidity was measured as the apparent absorbance at 550 nm (A_{550}) using a Cary 300 Bio spectrophotometer.[29] Dye-free polymer samples in BRAND semi-micro cuvettes were measured against matched buffer blanks during four heating–cooling cycles from 10 to 60 °C at 1 °C min^{-1}. Photographs were taken at 30, 40, 50, and 60 °C during heating at the same rate (Figures S12a–c). Differential scanning calorimetry was performed on four representative samples using a TA Instruments NanoDSC, with heating and cooling ramps at 1 °C min^{-1} under a constant pressure of 3 atm and subtraction of a matched pure-solvent blank, as an independent, label-free check on the transition temperatures (Section S8).

2.4 Dynamic light scattering and zeta-potential measurements

For DLS, 200 μL aliquots were loaded into BRAND UV microcuvettes and measured using a Malvern Zetasizer Nano ZSP in 173° backscatter mode. Samples equilibrated at room temperature were transferred to the instrument, which had been preset to the target temperature. 30 consecutive 30 s acquisitions were recorded without further equilibration, with 10 s between acquisitions. Because the turbid, evolving samples produced multiple scattering, collective flow, and sedimentation-driven number fluctuations, instrument-reported size distributions were not used. Analysis was restricted to the intensity autocorrelation function, $g^{(2)}(\tau) - 1$ (Section S10). Previous studies show that mesoglobule formation produces an approximately single-exponential correlation decay, consistent with a relatively monodisperse population, whereas floc formation produces a stretched decay associated with a broader, polydisperse population.[30]

Zeta potentials were measured in triplicate at 25 °C using the same instrument and folded capillary cells (DTS1070). Samples were equilibrated for 120 s, and zeta potentials were calculated from electrophoretic mobilities using the Smoluchowski approximation.

2.5 Optical microscopy and single-particle tracking

Three representative samples were examined by temperature-controlled dark-field microscopy during isothermal heating and stepwise cooling: citrate without added NaCl (C0; monotonic), citrate containing 1.0 M NaCl (C1; multistage), and borate containing 1.0 M NaCl (B1; monotonic). Droplet motion was analysed by single-particle tracking. Diffusion coefficients were obtained from the drift-insensitive pair-relative mean-squared displacement, $\mathrm{MSD}_{\mathrm{rel}}(\tau) = 8D\tau + b$, and converted to hydrodynamic diameters using the Stokes–Einstein relation and the temperature-dependent viscosity of each medium. Mean size is reported as the number-averaged hydrodynamic diameter, $\langle d_{\mathrm{H}} \rangle_{\mathrm{n}}$. Droplet count and integrated brightness were

used to monitor changes in population and relative scattering intensity, respectively. Full imaging, tracking, analysis, and validation details are provided in Section S9.

2.6 Analysis of fluorescence and turbidity traces

The first fluorescence cycle was excluded from quantitative analysis because it differed systematically from the later cycles. Cycles 2–4 were analysed independently, and transition temperatures are reported as mean ± SD. Cycle 2 is shown in the main figures; all cycles and the transition-temperature tables are provided in the Supporting Information (Section S5 for fluorescence and Section S7 for turbidity). Traces were interpolated onto a uniform temperature grid and smoothed using a second-order Whittaker algorithm. Heating profiles were classified as suppressed, monotonic, or multistage. Characteristic temperatures were obtained by segmented linear regression and verified independently from derivative extrema and intensity thresholds. Turbidity traces were plotted against temperature, and their transition and clearance temperatures were extracted using the same segmented-regression and derivative-based procedures. Full analysis details are provided in Section S5.

3. Results

3.1 Nile Red fluorescence

Nile Red fluorescence was recorded over four heating–cooling cycles for 12 conditions: citrate (pH 3), Tris (pH 7.4), and borate (pH 10), each containing 0–1.0 M NaCl (Figure 1). The first fluorescence cycle differed systematically from cycles 2–4 (Figure S9), whereas the turbidity traces were closely superimposable across successive cycles (Figure S11). Dye-only controls also showed a first-cycle difference (Figure S8a). The initial variation is therefore attributed mainly to equilibration of dye partitioning or its local environment, rather than to a major change in the aggregate population. Cycles 2–4 were reproducible, with standard deviations typically ≤0.5 °C, and all quantitative values below refer to these cycles (Table S5).

The heating traces showed three behaviours. (i) Multistage transitions occurred in citrate containing 0.5–1.0 M NaCl and in Tris containing 1.0 M NaCl; these traces showed an initial fluorescence rise, an extended plateau with a reduced slope, and a second rise at higher temperature. (ii) Monotonic transitions occurred under intermediate conditions, where fluorescence increased continuously without a resolved plateau. (iii) Borate containing 0–0.1 M NaCl showed no significant fluorescence increase, indicating no detectable formation of hydrophobic PNIPAM-rich domains. Characteristic temperatures for all conditions are listed in Table S5.

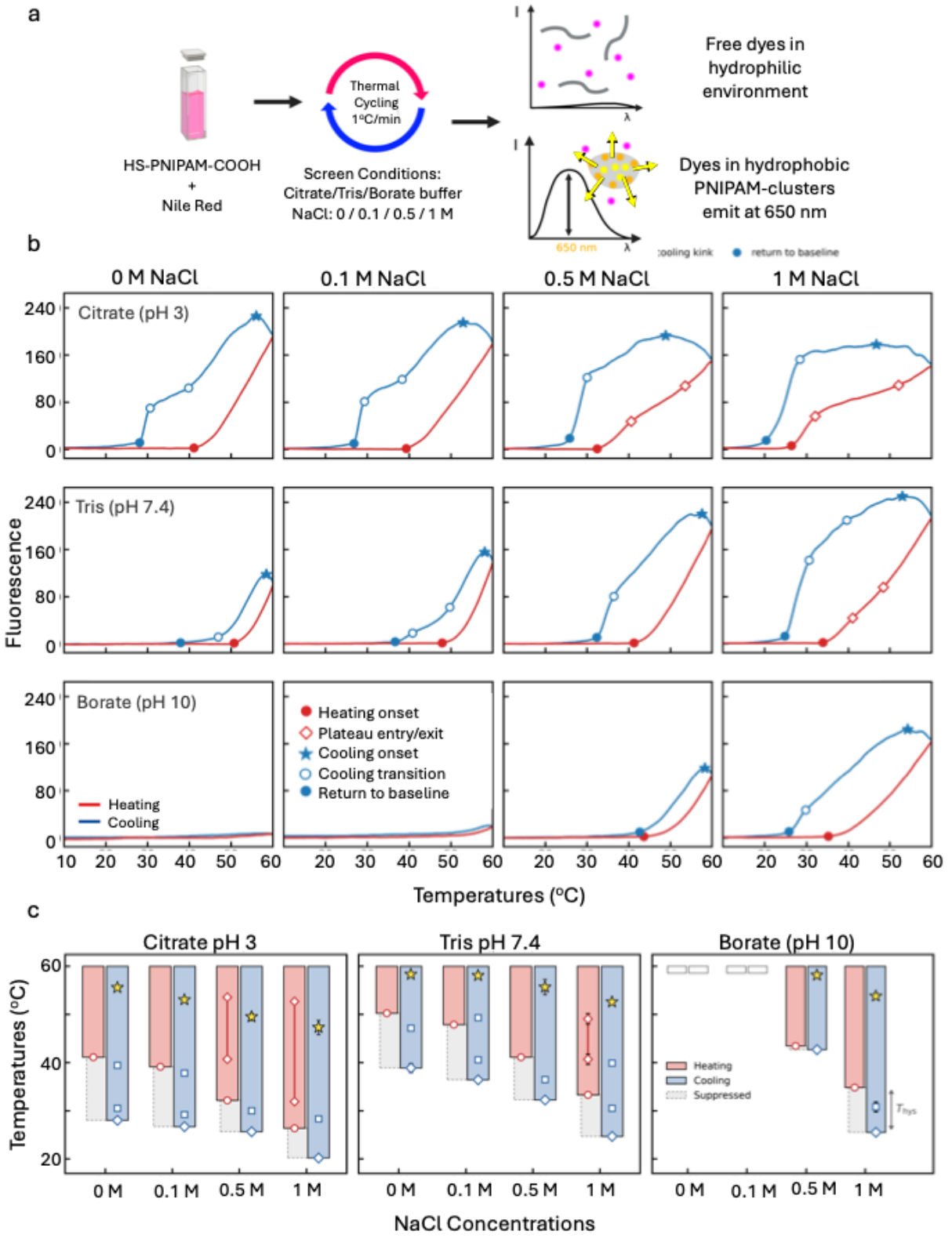


Figure 1. (a) Experimental workflow. Nile Red becomes strongly fluorescent after partitioning into hydrophobic PNIPAM-rich domains. (b) Nile Red fluorescence during cycle 2 in three buffers (pH measured at 25 °C; rows) and at four NaCl concentrations (columns). All thermal cycles are shown in Figure S9. (c) Characteristic temperatures extracted from cycles 2–4 (mean ± SD): red and blue bars span the heating and cooling branches, respectively, with symbols as in (b); the grey dashed box marks the hysteresis (ΔT_{hys}) between the heating onset and the cooling return to baseline; open boxes mark suppressed conditions.

Within the citrate and Tris series, the onset temperature decreased linearly with NaCl concentration ($R^2 \approx 0.99$), with slopes of −14.8 ± 1.0 and −16.4 ± 1.0 °C M^{-1}, respectively (Figure 1c). Their agreement indicates a similar salting-out sensitivity, while pH sets the baseline transition temperature: at a given NaCl concentration, the Tris onset was approximately 7–9 °C above that in citrate. Both slopes are steeper than the −10.3 °C M^{-1} reported for 6980 Da PNIPAM at 10 mg mL^{-1}.[14] At fixed NaCl concentration, the onset increased with pH, following the increasingly negative zeta potential measured without added NaCl: −1.9 ± 0.1 mV at pH 3, −23.2 ± 2.2 mV at pH 7.4, and −39.4 ± 0.5 mV at pH 10.

At 1.0 M NaCl, lowering the pH systematically broadened and flattened the fluorescence plateau (Figure 2). Additional measurements between pH 4.5 and 7.0 showed that the plateau width increased from 8.4 °C at pH 7.0 to 20.8 °C at pH 3.0, while its mean slope decreased from 4.4 to 2.3 a.u. $°C^{-1}$ (Table S6). The onset itself saturated below pH 4.5, reaching 26.1 ± 0.4 °C at pH 4.5 and 26.4 ± 0.0 °C at pH 3. The continued broadening at pH 3 therefore reflects evolution of the intermediate state rather than a further shift in the initial transition.

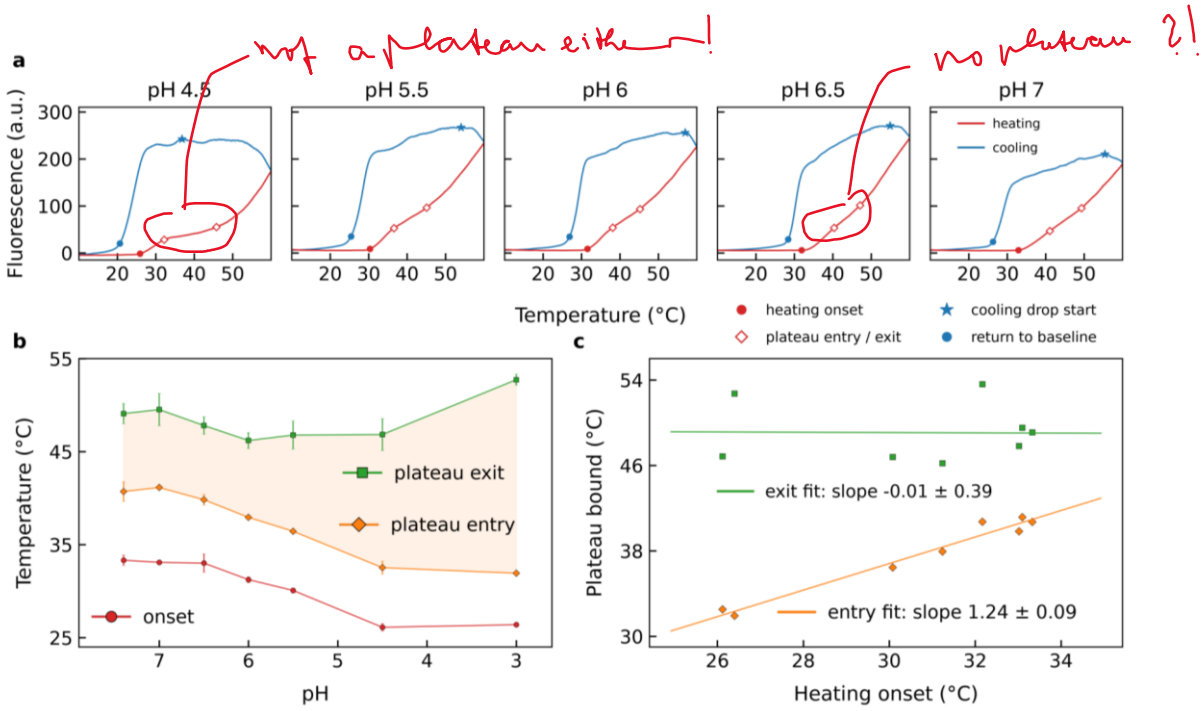


Figure 2. (a) Nile Red fluorescence for samples containing 1.0 M NaCl at pH 4.5–7.0 (cycle 2). (b) Onset, plateau-entry, and plateau-exit temperatures across pH 3–10 at 1.0 M NaCl. (c) Plateau-entry and plateau-exit temperatures plotted against the heating onset for all multistage conditions with linear fits. Characteristic temperatures are listed in Tables S5 and S6.

The two plateau boundaries responded differently to pH (Figure 2c). Plateau entry closely tracked the onset, with an average offset of 7.0 ± 1.0 °C across the eight multistage conditions and a regression slope of 1.24 ± 0.09 (R^2 = 0.97). By contrast, plateau exit was uncorrelated with onset (slope 0.0 ± 0.4). The plateau therefore broadened mainly through a downward shift of its entry temperature. The multistage pathway also had an upper pH boundary: borate containing 1.0 M NaCl showed a clear onset at 34.9 ± 0.4 °C, but its transition remained monotonic.

All non-suppressed conditions showed thermal hysteresis, and the shape of the fluorescence recovery varied among conditions. On cooling, samples with a distinct multistage transition exhibited an extended interval of slowly varying fluorescence before a sharp recovery at 28–31 °C (Table S5), whereas other samples recovered progressively. Within citrate, the fluorescence hysteresis decreased from 13.1 ± 0.2 °C without added NaCl to 6.2 ± 0.1 °C at 1.0 M NaCl; in Tris it decreased from 11.4 ± 1.3 to 8.6 ± 0.5 °C. This narrowing arose because the heating onset was more salt-sensitive than the cooling clearance. Borate showed the opposite trend: the hysteresis increased from 0.7 ± 0.3 °C at 0.5 M NaCl to 9.3 ± 0.2 °C at 1.0 M NaCl.

3.2 Turbidimetry

Turbidity at 550 nm (A_{550}) is shown with Nile Red fluorescence in Figure 3. We find that A_{550} followed the same ordering across conditions as the fluorescence, with cycle-to-cycle reproducibility typically within ±0.3 °C (Figure 3; Table S7). Unlike fluorescence, the first turbidity cycle generally overlapped with the later cycles, which supports the assignment of the first-cycle fluorescence change to dye equilibration rather than to a change in the aggregate population. Borate containing 0 or 0.1 M NaCl produced no measurable turbidity in any cycle, independently supporting its classification as suppressed.

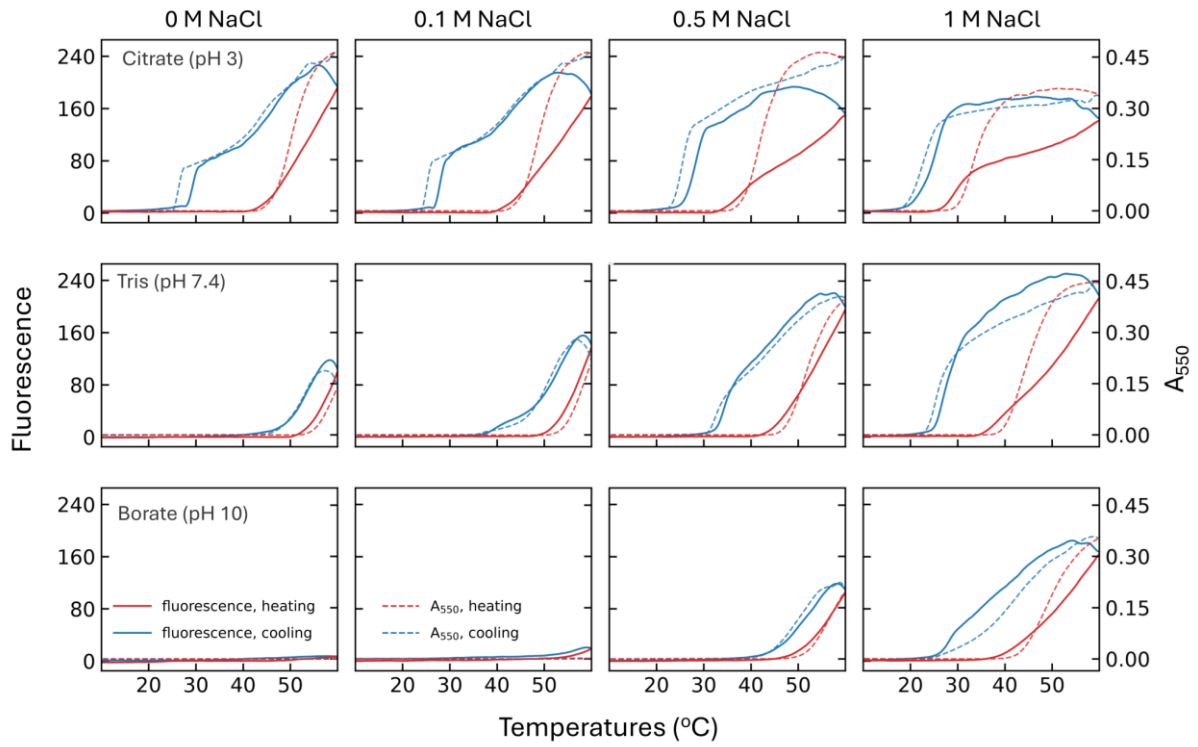


Figure 3. Baseline-corrected apparent absorbance at 550 nm (A_{550}, dashed lines) during heating and cooling for all buffer and NaCl conditions, overlaid with the corresponding Nile Red fluorescence traces (solid lines). Cycle 2 is shown; all cycles are given in Figure S11.

During heating, turbidity onsets occurred systematically above the corresponding fluorescence onsets (Figure 4a), and the offset increased with NaCl concentration at every pH. Local dehydration therefore precedes the formation of optically resolvable scatterers. Turbidity showed no resolved multistage rise. Instead, it continued to increase across the fluorescence plateau and approached saturation near the onset of the second fluorescence rise. In citrate containing 0.5 and 1.0 M NaCl, the absorbance reached maxima at 54.7 and 51.8 °C, respectively, close to the plateau exit, before decreasing by 3.3% and 3.2% by the end of heating.

The turbidity hysteresis exceeded the fluorescence hysteresis by approximately 3–8 °C under nearly all conditions (Figure 4c). In citrate, the turbidity hysteresis also narrowed with added salt, from 18.8 ± 0.2 °C without added NaCl to 12.1 ± 0.2 °C at 1.0 M NaCl, whereas in Tris it remained near 14.8 °C between 0.1 and 1.0 M NaCl. Borate showed the opposite salt dependence: from 0.5 to 1.0 M NaCl, the turbidity hysteresis increased from 5.6 ± 1.1 to 15.8 ± 0.2 °C.

The order of fluorescence and turbidity recovery during cooling also varied systematically (Figure 4b). In citrate, turbidity persisted 2.4–4.6 °C below the fluorescence clearance at every NaCl concentration, showing that local rehydration began before the large scatterers disappeared. In high-salt Tris and in borate at 0.5 M NaCl, the offset was smaller, whereas in Tris at 0.1 M NaCl and in borate at 1.0 M NaCl the two clearances coincided within experimental uncertainty. The decreasing offset with increasing end-group ionisation is consistent with charge facilitating aggregate disassembly more strongly than it changes the local fluorescence clearance. Differential scanning calorimetry on four representative samples was consistent with these assignments: a heating endotherm began near the fluorescence onset and a cooling exotherm coincided with the fast fluorescence collapse, although at this polymer concentration the excess heat rate of 1–7 μJ s^{-1} is comparable to the baseline drift, so the intermediate stages are not resolved (Section S8, Figure S13).

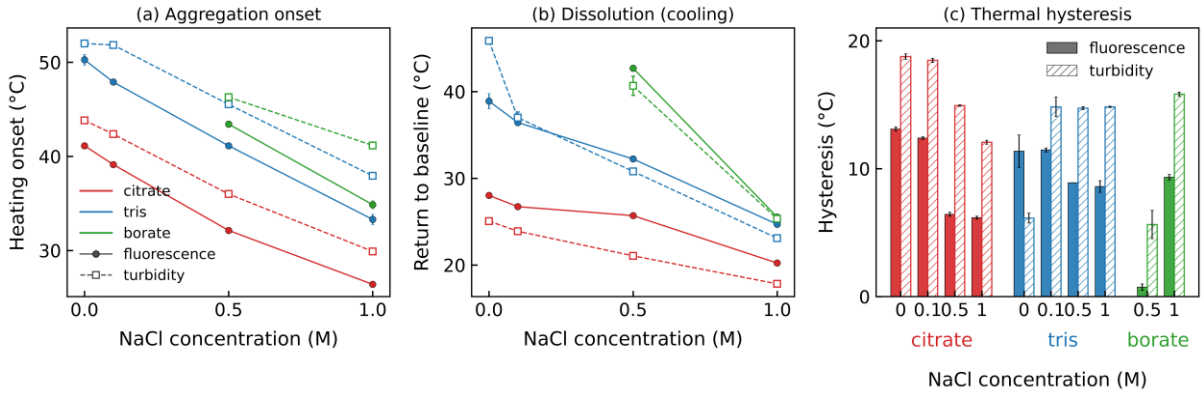


Figure 4. Comparison of fluorescence (filled circles) and turbidity (open squares) transition temperatures (cycles 2–4, mean ± SD; Tables S5 and S7). (a) Heating onset and (b) return to baseline on cooling, as a function of NaCl concentration. (c) Thermal hysteresis (heating onset minus cooling clearance) from fluorescence (filled bars) and turbidity (dashed bars).

3.3 Direct microscopy of mesoglobule growth and dissolution

Single-particle tracking was used to compare two monotonic conditions, citrate without added NaCl (C0) and borate containing 1.0 M NaCl (B1), with the multistage condition, citrate containing 1.0 M NaCl (C1). No optically resolved droplets were detected below the transition onset. Above it, droplets appeared within the first few minutes and were quantified by droplet

count, per-droplet brightness, total scattered intensity, and number-averaged hydrodynamic diameter, $\langle d_H \rangle_n$ (Figures 5 and 6).

C0 and B1 both showed continuous growth during isothermal holds above their onsets (Figure 5a,b). Near the onset, nucleation continued while existing droplets grew; for C0 at 43 °C, the count increased from approximately 1 to 60 droplets per frame while $\langle d_H \rangle_n$ increased from 0.57 to 0.67 μm (+19%). Deeper temperature jumps produced an initial nucleation burst followed by declining droplet counts but continued size increases. For C0, $\langle d_H \rangle_n$ increased by 15–46% between 50 and 60 °C, whereas B1 showed stronger growth of 36–61% between 45 and 60 °C. In both samples, the total scattered intensity decreased more slowly than the droplet count, the surviving droplets became progressively brighter, and the entire size distribution shifted towards larger diameters rather than changing through removal of its small-particle tail. Most resolved droplet encounters also ended in separation (Supplementary S9.5).

C1 behaved differently (Figure 5c). Immediately above the onset at 28 °C, nucleation continued throughout the hold: the count increased from approximately 30 to 350 droplets per frame while $\langle d_H \rangle_n$ increased from 0.94 to 1.09 μm (+15%). Following rapid jumps to temperatures between 32 and 50 °C, however, the droplets formed close to their final size within the first analysis window and showed no growth, with $\langle d_H \rangle_n$ decreasing slightly during each hold (by −1 to −7%, and by approximately −11% at 35 °C). Sustained growth returned only at 60 °C, where $\langle d_H \rangle_n$ increased from 1.00 to 1.17 μm (+16%). The stable-size interval approximately coincided with the fluorescence plateau, whereas renewed growth occurred beyond the plateau, during the second fluorescence rise.

Although C1 droplets did not grow during the plateau holds, their initial size varied non-monotonically, reaching 1.24 μm at 32 °C, a maximum of 1.54 μm at 35 °C, and 1.04–1.26 μm at 45 and 50 °C. This variation was broadly anticorrelated with the initial population of 430–750 droplets per frame, indicating that deeper jumps generally produce more, smaller

droplets. During each hold, the total scattered intensity fell at approximately the same rate as the droplet count, and the brightness of the surviving droplets did not change. This behaviour indicates loss of dense droplets through sedimentation. A vertical scan at 60 °C confirmed this interpretation: approximately 15-fold more droplets were present near the substrate than in the bulk, with 47-fold greater total intensity and approximately 4-fold greater individual brightness (Figure S19).

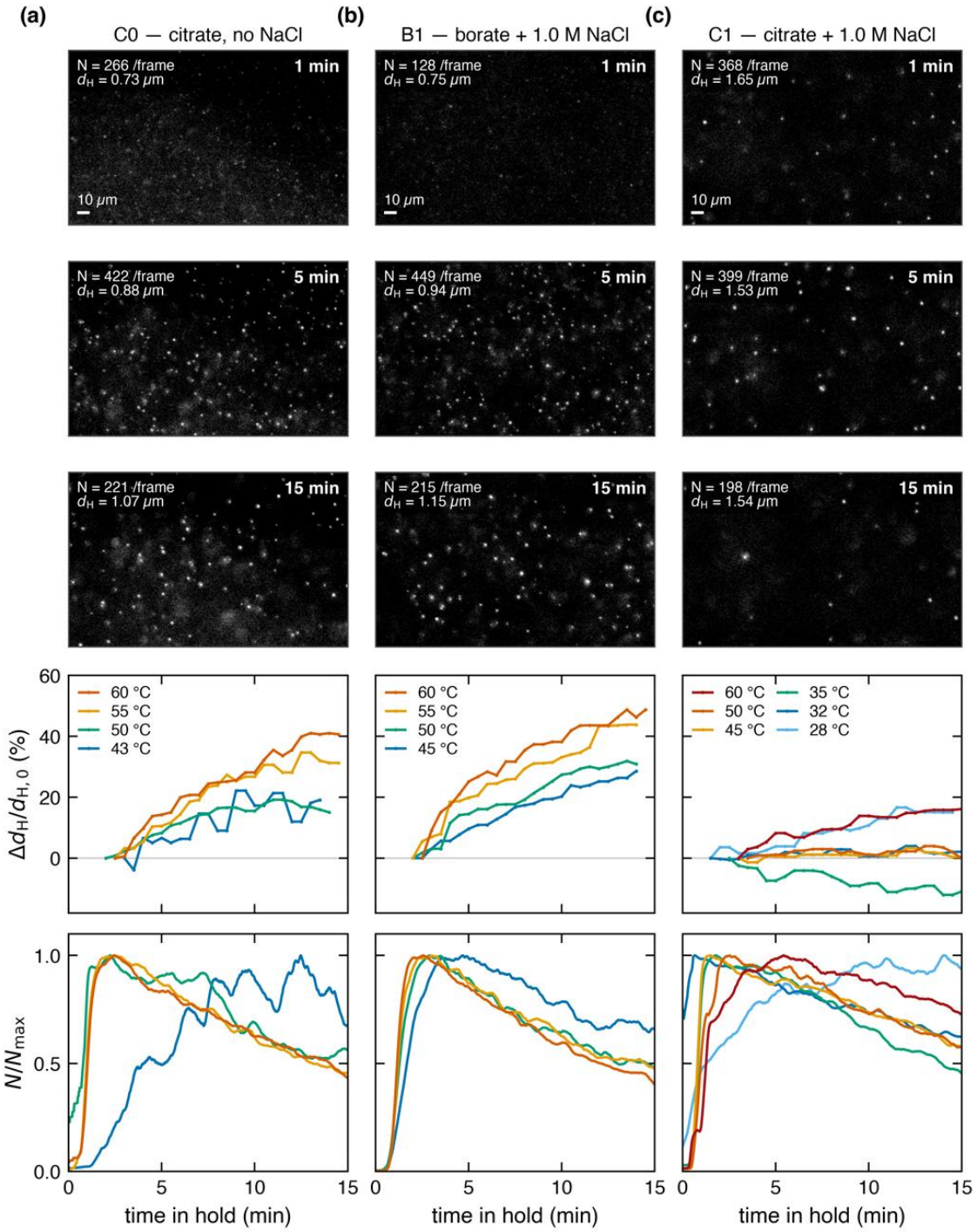


Figure 5. Dark-field microscopy of droplet growth during isothermal holds after temperature jumps: (a) C0 at 60 °C, (b) B1 at 60 °C, and (c) C1 at 35 °C. Top: 221 × 138 μm sub-fields at 1, 5, and 15 min. Bottom: relative change in $\langle d_H \rangle_n$ and normalised droplet count for all hold temperatures.

Cooling also distinguished the monotonic and multistage pathways. Following shallow cooling, both monotonic samples showed gradual droplet shrinkage (Figure 6a,b). For C0, cooling from 60 to 40 °C reduced $\langle d_H \rangle_n$ from 0.89 to 0.70 μm (−21%) over 15 min, while the count decreased from 135 to 63 droplets per frame. For B1, cooling to 45 °C reduced $\langle d_H \rangle_n$ by

11%, whereas cooling to 35 °C produced an 18% decrease (0.79 to 0.65 µm). Further cooling to 25 °C removed the C0 and B1 populations within 1 min.

C1 again followed a distinct pathway (Figure 6c). Cooling from 60 to 40 °C left $\langle d_H \rangle_n$ nearly unchanged at approximately 1.05 µm, while the count increased from approximately 230 to 400 droplets per frame within the first minute. The newly detected droplets were dimmer than the pre-existing population but comparable in size to droplets formed directly at 40 °C, suggesting that partial rehydration lowered the density of previously sedimented droplets and returned part of that population to the observation volume. After further cooling to 25 °C, the population remained stable for approximately 75 s, with $\langle d_H \rangle_n$ remaining at 0.87–0.89 µm, before collapsing from 206 to 4 droplets per frame within approximately 30 s. This collapse was essentially population-wide: 92% of tracked droplets disappeared simultaneously.

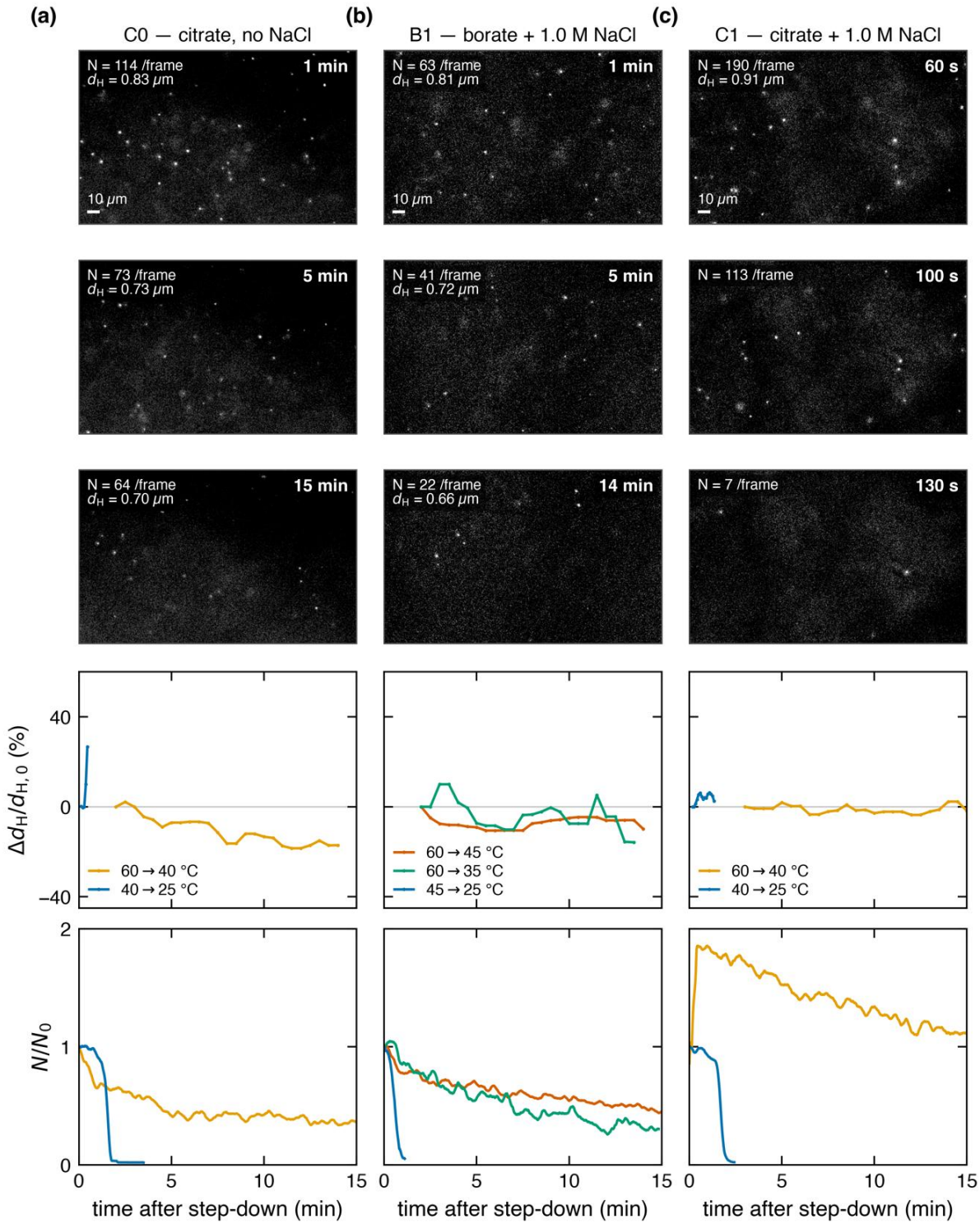


Figure 6. As in Figure 5, for (a) C0 cooled 60→40 °C, (b) B1 cooled 60→35 °C, and (c) C1 cooled 40→25 °C. Bottom: relative change in $\langle d_H \rangle_n$ and normalised droplet count for all cooling steps.

3.4 Dynamic light scattering

Isothermal DLS measurements provided an ensemble-level comparison with the 15 min microscopy holds. Correlation-function series for each hold are shown in Figure S23. Below

its transition, C1 produced weak correlations without a well-defined decay. Above the onset, C1 at 30 °C showed stretched, time-dependent decays, indicating broad relaxation-time distributions and continuing structural evolution. C0 and B1 at 50 °C also showed continuously evolving, stretched and oscillating correlation functions during the hold, consistent with the sustained droplet growth and broad size distributions.

When C1 was jumped further into the plateau region (35 and 40 °C), the first few correlation functions were irregular, with fluctuating intercepts and decay shapes during formation of the scattering population. They subsequently converged to reproducible, single-step decays that remained nearly unchanged for the rest of the hold, supporting a stationary plateau state. At 50 and 60 °C, the correlations became stretched and developed oscillations, indicating renewed population dynamics. Notably, 50 °C lies near the plateau exit and showed different signatures in DLS and microscopy: DLS detected non-stationary dynamics, whereas microscopy showed no measurable growth of the resolved droplets. This difference may arise because DLS is sensitive to sub-resolution rearrangements, polydispersity, and directed motion that do not necessarily produce a measurable change in the mean size of the resolved droplets. Overall, DLS independently supports continued evolution in C0 and B1 at 50 °C, a stationary C1 state at 35–40 °C, and renewed C1 dynamics at and beyond the plateau boundary.

4. Discussion

The combined measurements show that pH and NaCl select distinct phase-separation behaviours in heterotelechelic HS–PNIPAM–COOH. The fluorescence onset marks the initial dehydration and formation of locally hydrophobic PNIPAM-rich domains, whereas the subsequent fluorescence, turbidity, microscopy, and DLS responses describe how these domains develop once phase separation has begun. The multistage, monotonic, and suppressed responses therefore represent distinct pathways selected by the balance among end-group ionisation, electrostatic screening, dehydration, and interfacial chain relaxation (Figure 7).

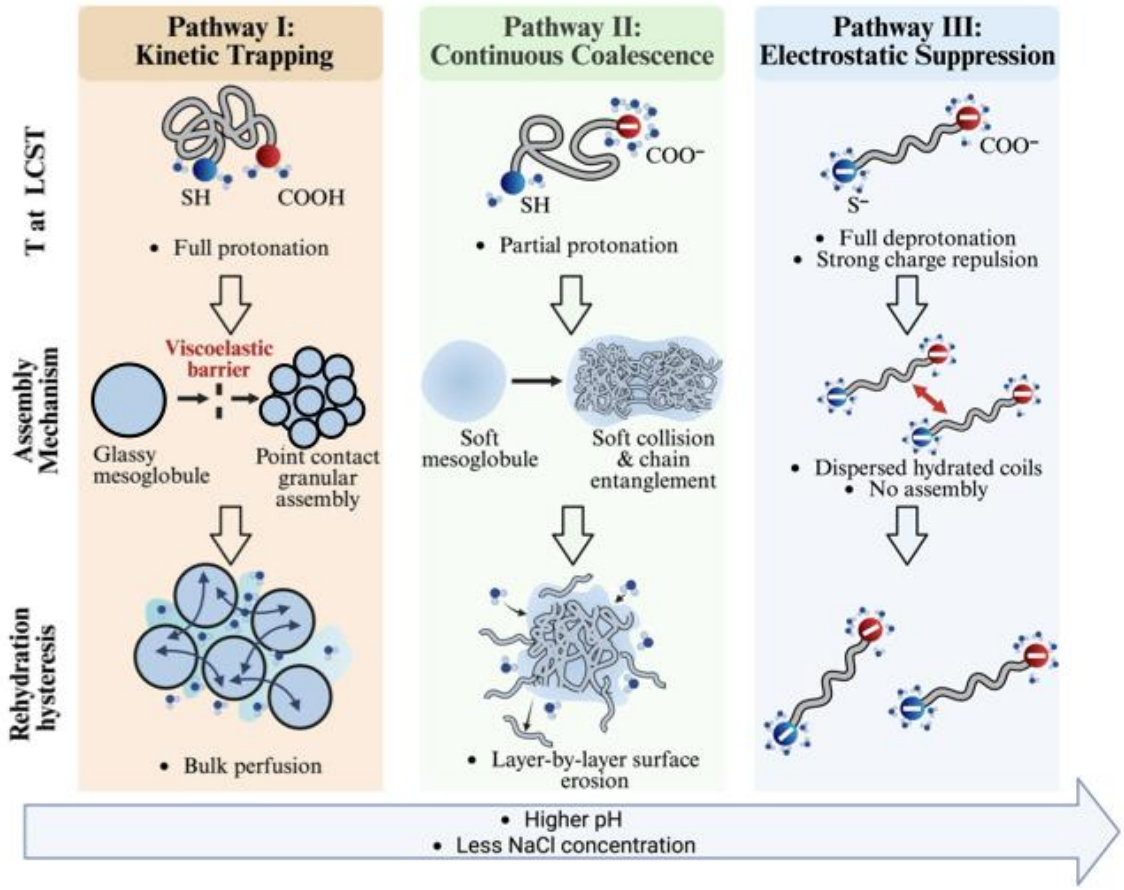


Figure 7. Proposed pH- and NaCl-dependent phase-separation pathways of HS–PNIPAM–COOH. In Pathway I (multistage, e.g., citrate with 1.0 M NaCl), rapid dehydration creates a densified, viscoelastic interface that arrests growth until further heating; dissolution during cooling is delayed and collective. In Pathway II (monotonic, e.g., citrate without added NaCl and borate with 1.0 M NaCl), mobile interfaces allow continuous growth from a reservoir of sub-resolution clusters and gradual chain release during cooling before final dissolution. In Pathway III (suppressed, e.g., borate with 0 or 0.1 M NaCl), strongly ionized, weakly screened chains do not form detectable mesoscopic assemblies. Sizes are not scalable for representation purpose.

4.1 Coupled roles of pH and NaCl in pathway selection

The fluorescence onset increased with pH. Because the PNIPAM repeat units are not ionised over this range, this trend is attributed to progressive ionisation of the terminal carboxyl and thiol groups, which enhances end-group hydration and electrostatic repulsion and thereby delays the earliest detectable dehydration event. In the extended 1.0 M NaCl series, the onset remained constant below pH 4.5 and increased primarily between pH 4.5 and 6.5, consistent with deprotonation of the carboxyl terminus ($pK_a \approx 4–5$) as the dominant pH-dependent contribution.[23] At pH 10, thiol ionisation may contribute to the further onset increase and to the pronounced change in macroscopic association.[24] Under weak screening, ionisation of both

termini suppressed detectable interchain association, although intrachain collapse below the detection limit cannot be excluded.

NaCl lowered the fluorescence onset with comparable slopes in citrate and Tris, consistent with salting-out of the PNIPAM backbone rather than an ionisation-specific effect.[13,14] Its screening role was most apparent at high pH: the borate series progressed from no detectable transition at 0–0.1 M NaCl, to partial aggregation at 0.5 M, and to strongly hysteretic aggregation at 1.0 M. The increasing separation between the fluorescence and turbidity onsets further indicates that local dehydration and nanoscale-domain formation are more salt-sensitive than their subsequent development into optically resolvable particles. Salt therefore promotes initial collapse and association, whereas later coarsening remains limited by particle encounters and interfacial rearrangement.

Electrostatic screening alone, however, cannot explain pathway selection. Pronounced pH dependence persisted at 1.0 M NaCl, where the Debye screening length is approximately 0.3 nm: lowering the pH progressively broadened and flattened the fluorescence plateau, whereas the borate response remained monotonic. This residual dependence indicates that local end-group hydration and interfacial mobility remain important even when long-range electrostatic interactions are strongly screened. Hydrated, ionised termini may maintain a softer and more mobile interface, favouring continuous growth once association becomes possible. By contrast, protonated termini combined with strong NaCl-induced dehydration may promote rapid interfacial densification and kinetic arrest. The transition from continuous to multistage profiles between 0 and 1.0 M NaCl at pH 7.4 (Figures 1 and 2) illustrates how increasing salt shifts the balance from sustained coarsening towards kinetically hindered growth.

4.2 Multistage pathway: kinetic trapping by dehydration-driven interfacial densification

C1 provides the clearest evidence that the multistage response represents a distinct aggregation pathway. During the fluorescence plateau, the mean mesoglobule size remained

nearly constant and the DLS correlations at 35–40 °C became stationary, whereas turbidity continued to increase . This combination indicates structural evolution without substantial particle growth.

We propose that low pH and high NaCl accelerate PNIPAM dehydration, causing chains to collapse rapidly into globules or small polymer-rich clusters. During collisions, chain relaxation may be too slow for complete interpenetration and fusion, producing loosely connected, fractal-like assemblies.[31] Time-resolved SANS identified an analogous progression from transient fractal clusters to compact mesoglobules whose stiff surfaces limit further particle growth.[10,11,32] This behaviour is also compatible with topological repulsion between collapsed globules[33] and with the reported fluid-to-rigid transition of PNIPAM particles.[8] Continued dehydration may densify the outer regions and the interdomain contacts, arresting further coalescence while retaining water-filled interstitial regions.

This structure accounts for the different fluorescence and turbidity responses. Nile Red reports the local polarity of the dehydrated polymer-rich domains, so its fluorescence may plateau soon after these domains form. Turbidity, by contrast, remains sensitive to particle-scale density and refractive-index contrast; continued expulsion of interstitial water could thus increase turbidity without changing fluorescence or mean particle size. The combined measurements therefore support progressive densification of porous, incompletely fused mesoglobules during the plateau (Figure 7, Pathway I), although direct confirmation would require time-resolved SANS or SAXS.

At higher temperature, the second fluorescence increase coincided with renewed microscopic growth and evolving DLS correlation functions, marking escape from the arrested state. A deeper thermal quench increases the thermodynamic driving force for polymer-rich contacts and may enable repeated encounters to overcome the barrier to interfacial rearrangement. The accompanying oscillatory DLS correlations indicate collective motion,[34] while the

turbidity maximum and subsequent decrease are consistent with sedimentation and loss of large particles from the measurement volume.

The distinct cooling response further supports this pathway. C1 remained near 1.05 μm after cooling to 40 °C and persisted transiently at 25 °C before dissolving collectively (§3.3). Fluorescence returned to baseline before turbidity, indicating local rehydration before complete particle disassembly. Such persistence is consistent with the established hysteresis of PNIPAM collapse and rehydration,[35] which has been associated with intrachain structures formed in the collapsed state[36] and with intersegment hydrogen bonds that act as transient physical cross-links within aggregates.[37] A densified interface could therefore permit water entry while restricting chain escape, allowing internal rehydration or swelling before the particle loses its integrity and dissolves collectively. We describe this mechanism tentatively as permeation-driven rehydration, by analogy with the swelling-dominated disintegration reported under strong osmotic driving forces.[12] The arrested plateau during heating and the delayed, collective dissolution during cooling can thus be explained by the same structural feature: a densified interface that restricts both further coalescence and gradual chain release.

4.3 Monotonic pathway: reservoir-fed growth and surface-limited rehydration

C0 and B1 followed a different growth pathway. Following the initial nucleation burst, deeper temperature jumps produced faster, sustained growth, and the surviving droplets became larger and brighter while their detected numbers decreased. Direct tracking, however, showed that collisions between resolved droplets rarely resulted in fusion (Figure S22). Instead, the persistence of the total scattered intensity as the resolved count fell suggests continuous transfer of polymer to the droplets from a reservoir of sub-resolution clusters and coalescence involving unresolved material. This growth mode resembles classical coarsening, in which larger domains grow at the expense of smaller ones through the surrounding phase.[38,39] It also resembles the diffusion-limited coalescence of small mesoglobules observed by kinetic

SANS.[11,32] Such a growth mode is plausible when dehydration is relatively slow, as in C0 without added NaCl, or when hydrated, ionised termini maintain interfacial mobility, as in B1. The closely coupled evolution of fluorescence, turbidity, and particle size during heating is consistent with continuous coupling between dehydration and growth (Figure 7, Pathway II). This contrasts with C1, where droplet size and brightness remained nearly constant through the plateau while the resolved count and total intensity declined in parallel.

Cooling provided complementary evidence for continuous interfacial exchange. C0 and B1 droplets shrank gradually during shallow cooling, with the size distribution shifting towards smaller diameters. Turbidity recovered before the extended fluorescence tail disappeared, indicating that mesoscale structures disassembled while smaller PNIPAM-rich regions remained partially dehydrated. This behaviour is analogous to the gradual release of chains from mesoglobule surfaces reported under weak osmotic driving forces[12] and is therefore described tentatively as surface-limited rehydration. Sequential uptake during heating may produce a compact, older interior surrounded by more recently incorporated and less strongly interpenetrated material, allowing the peripheral material to be released first during cooling. This internal hierarchy remains a working model rather than a directly resolved structure.

5. Conclusions

We used solvatochromic Nile Red fluorescence together with turbidimetry, DLS and dark-field imaging to examine how end-group ionization and NaCl concentration regulate the phase separation of heterotelechelic HS–PNIPAM–COOH ($M_n \approx 6$ kDa). Across different combinations of pH and salt, three distinct behaviours are identified: (i) suppressed transitions under strongly ionized and weakly screened conditions, (ii) monotonic transitions under intermediate conditions, and (iii) a multistage transition with long-lived mesoglobule intermediates at low pH and/or high NaCl. The distinct cooling behaviours between the monotonic and multistage regimes constitutes the most direct evidence that these pathways produce structurally

distinct high-temperature states. We propose that pH sets the baseline hydration and interfacial mobility of PNIPAM-rich domains through end-group ionization, while NaCl both screens residual electrostatic repulsion and accelerates dehydration. When dehydration outpaces interfacial relaxation, mesoglobules become kinetically trapped due to a viscoelastic barrier to coalescence.

These findings suggest several directions for future work. Scattering techniques with structural resolution (particularly time-resolved SANS or SAXS) could directly test the proposed interfacial densification mechanism by probing mesoglobule radial density profiles under different pH–salt conditions. Extending the approach to PNIPAM of higher molecular weight, different architectures, or alternative ionizable end-groups would clarify the generality of the pathway-selection framework. More broadly, the ability to select among kinetically distinct pathways using only pH and salt concentration should prove useful for applications in which mesoglobule lifetime is a critical design parameter.

Supporting Information

Polymer molecular-weight characterisation by SEC and NMR, the concentration-dependent cloud point in pure water, and the effect of purification by precipitation (S1); TCEP controls (S2); buffer pH–temperature profiles and MOPS comparison (S3); Nile Red concentration and dye-only controls (S4); all fluorescence thermal cycles, the transition-temperature analysis, and tabulated characteristic temperatures (S5); the extended pH series at 1.0 M NaCl (S6); all turbidity thermal cycles, turbidity transition temperatures, and sample photographs (S7); differential scanning calorimetry (S8); optical microscopy and single-particle-tracking methods, validation, vertical sedimentation profile, and Movies S1–S5 (S9); and DLS correlation functions with buffer-only controls (S10).

Acknowledgments

The authors acknowledge financial support from the European Research Council (ERC) under the Horizon 2020 research and innovation programme, grants PICOFORCE (No. 883703) and POSEIDON (No. 861950), and from the EPSRC (Cambridge NanoDTC EP/L015978/1, EP/L027151/1, EP/X037770/1). TTS. was supported by the Data-Piets Fonds. YZ was supported by Cambridge Trust and George and Lillian Schiff Studentship. Claude was used for data analysis and paper editing.

Author Contributions

YZ, TTS, and JJB conceived and designed the experiments. YZ performed the experiments with support from TTS and carried out the data analysis. YZ, JJB, and UFK developed the mechanistic interpretation. TX and RKO assisted with the chemical characterization of the polymer, and JQ assisted with setting up the microscopy imaging experiments. All authors contributed to writing, reviewing, and editing the manuscript.

Competing Interests

The authors declare no competing interests.

Data Availability

Data supporting this study are provided in the article and its Supporting Information.

References

1. Halperin, A., M. Kröger, and F.M. Winnik, *Poly(N-isopropylacrylamide) Phase Diagrams: Fifty Years of Research.* Angewandte Chemie International Edition, 2015. **54**(51): p. 15342-15367.
2. Wu, C. and S. Zhou, *Laser Light Scattering Study of the Phase Transition of Poly(N-isopropylacrylamide) in Water. 1. Single Chain.* Macromolecules, 1995. **28**(24): p. 8381-8387.
3. Aseyev, V., et al., *Mesoglobules of thermoresponsive polymers in dilute aqueous solutions above the LCST.* Polymer, 2005. **46**(18): p. 7118-7131.

4. Chan, K., R. Pelton, and J. Zhang, *On the Formation of Colloidally Dispersed Phase-Separated Poly(N-isopropylacrylamide).* Langmuir, 1999. **15**(11): p. 4018-4020.

5. Gorelov, A.V., A. Du Chesne, and K.A. Dawson, *Phase separation in dilute solutions of poly(N-isopropylacrylamide).* Physica A: Statistical Mechanics and its Applications, 1997. **240**(3-4): p. 443-452.

6. Haladjova, E., et al., *Polymeric Nanoparticle Engineering: From Temperature-Responsive Polymer Mesoglobules to Gene Delivery Systems.* Biomacromolecules, 2014. **15**(12): p. 4377-4395.

7. Ji, D., et al., *Sustainable 3D printing by reversible salting-out effects with aqueous salt solutions.* Nature Communications, 2024. **15**(1): p. 3925.

8. Kujawa, P., et al., *Temperature-Sensitive Properties of Poly(N-isopropylacrylamide) Mesoglobules Formed in Dilute Aqueous Solutions Heated above Their Demixing Point.* Macromolecules, 2006. **39**(22): p. 7686-7693.

9. Papadakis, C.M., B.-J. Niebuur, and A. Schulte, *Thermoresponsive Polymers under Pressure with a Focus on Poly(N-isopropylacrylamide) (PNIPAM).* Langmuir, 2024. **40**(1): p. 1-20.

10. Niebuur, B.-J., et al., *PNIPAM Mesoglobules in Dependence on Pressure.* Langmuir, 2024. **40**(42): p. 22314-22323.

11. Niebuur, B.-J., et al., *Kinetics of Mesoglobule Formation and Growth in Aqueous Poly(N-isopropylacrylamide) Solutions: Pressure Jumps at Low and at High Pressure.* Macromolecules, 2019. **52**(17): p. 6416-6427.

12. Niebuur, B.-J., et al., *Nanoscale disintegration kinetics of mesoglobules in aqueous poly(N-isopropylacrylamide) solutions revealed by small-angle neutron scattering and pressure jumps.* Nanoscale, 2021. **13**(31): p. 13421-13426.

13. Burba, C.M., et al., *Salt Effects on Poly(N-isopropylacrylamide) Phase Transition Thermodynamics from NMR Spectroscopy.* The Journal of Physical Chemistry B, 2008. **112**(34): p. 10399-10404.

14. Zhang, Y., et al., *Effects of Hofmeister Anions on the LCST of PNIPAM as a Function of Molecular Weight.* The Journal of Physical Chemistry C, 2007. **111**(25): p. 8916-8924.

15. Furyk, S., et al., *Effects of end group polarity and molecular weight on the lower critical solution temperature of poly(N-isopropylacrylamide).* Journal of Polymer Science Part A: Polymer Chemistry, 2006. **44**(4): p. 1492-1501.

16. Xia, Y., N.A.D. Burke, and H.D.H. Stöver, *End Group Effect on the Thermal Response of Narrow-Disperse Poly(N-isopropylacrylamide) Prepared by Atom Transfer Radical Polymerization.* Macromolecules, 2006. **39**(6): p. 2275-2283.

17. Qiu, X., et al., *New insights into the effects of molecular weight and end group on the temperature-induced phase transition of poly(N-isopropylacrylamide) in water.* Science China Chemistry, 2013. **56**(1): p. 56-64.

18. Sharker, K.K., et al., *pH- and thermo-responsive behavior of PNIPAM star containing terminal carboxy groups in aqueous solutions.* Polymer, 2020. **203**: p. 122735.

19. Hummer, G., L.R. Pratt, and A.E. García, *Free Energy of Ionic Hydration.* The Journal of Physical Chemistry, 1996. **100**(4): p. 1206-1215.

20. Weng, Y., Y. Ding, and G. Zhang, *Microcalorimetric Investigation on the Lower Critical Solution Temperature Behavior of N-Isopropycrylamide-co-Acrylic Acid Copolymer in Aqueous Solution.* The Journal of Physical Chemistry B, 2006. **110**(24): p. 11813-11817.

21. Yin, X., A.S. Hoffman, and P.S. Stayton, *Poly(N-isopropylacrylamide-co-propylacrylic acid) Copolymers That Respond Sharply to Temperature and pH.* Biomacromolecules, 2006. **7**(5): p. 1381-1385.

22. Locatelli-Champagne, C. and M. Cloitre, *Monitoring mesoglobules formation in PNIPAm solutions using Nile Red solvatochromism.* Colloid and Polymer Science, 2013. **291**(12): p. 2911-2916.

23. Škvarla, J., et al., *Thermoresponsive behavior of poly(N-isopropylacrylamide)s with dodecyl and carboxyl terminal groups in aqueous solution: pH-dependent cloud point temperature.* Colloid and Polymer Science, 2017. **295**(8): p. 1343-1349.

24. Beaupre, D.M. and R.G. Weiss, *Thiol- and Disulfide-Based Stimulus-Responsive Soft Materials and Self-Assembling Systems.* Molecules, 2021. **26**(11): p. 3332.

25. Getz, E.B., et al., *A comparison between the sulfhydryl reductants tris(2-carboxyethyl)phosphine and dithiothreitol for use in protein biochemistry.* Analytical Biochemistry, 1999. **273**(1): p. 73-80.

26. Visser, C.C., et al., *Coupling of metal containing homing devices to liposomes via a maleimide linker: use of TCEP to stabilize thiol-groups without scavenging metals.* Journal of Drug Targeting, 2004. **12**(9-10): p. 569-573.

27. Bruce, E.E., et al., *Nonadditive Ion Effects Drive Both Collapse and Swelling of Thermoresponsive Polymers in Water.* Journal of the American Chemical Society, 2019. **141**(16): p. 6609-6616.

28. Yan, X., et al., *Dynamic mechanism of halide salts on the phase transition of protein models, poly(N-isopropylacrylamide) and poly(N,N-diethylacrylamide).* Physical Chemistry Chemical Physics, 2020. **22**(22): p. 12644-12650.

29. Li, Y., G. Wang, and Z. Hu, *Turbidity Study of Spinodal Decomposition of an N-Isopropylacrylamide Gel.* Macromolecules, 1995. **28**(12): p. 4194-4197.

30. Bischofberger, I. and V. Trappe, *New aspects in the phase behaviour of poly-N-isopropyl acrylamide: systematic temperature dependent shrinking of PNiPAM assemblies well beyond the LCST.* Scientific Reports, 2015. **5**: p. 15520.

31. Tanaka, H., *Viscoelastic phase separation.* Journal of Physics: Condensed Matter, 2000. **12**(15): p. R207-R264.

32. Niebuur, B.-J., et al., *Formation and Growth of Mesoglobules in Aqueous Poly(N-isopropylacrylamide) Solutions Revealed with Kinetic Small-Angle Neutron Scattering and Fast Pressure Jumps.* ACS Macro Letters, 2018. **7**(10): p. 1155-1160.

33. Chuang, J., A.Y. Grosberg, and T. Tanaka, *Topological repulsion between polymer globules.* The Journal of Chemical Physics, 2000. **112**(14): p. 6434-6442.

34. López-Molina, J., A. Moncho-Jordá, and M. Tirado-Miranda, *Measuring Absolute Velocities from Nonequilibrium Oscillations via Single-Detector 3D Dynamic Light Scattering.* Physical Review Letters, 2024. **133**(19): p. 198202.

35. Van Durme, K., G. Van Assche, and B. Van Mele, *Kinetics of Demixing and Remixing in Poly(N-isopropylacrylamide)/Water Studied by Modulated Temperature DSC.* Macromolecules, 2004. **37**(25): p. 9596-9605.

36. Wang, X., X. Qiu, and C. Wu, *Comparison of the Coil-to-Globule and the Globule-to-Coil Transitions of a Single Poly(N-isopropylacrylamide) Homopolymer Chain in Water.* Macromolecules, 1998. **31**(9): p. 2972-2976.

37. Cheng, H., L. Shen, and C. Wu, *LLS and FTIR Studies on the Hysteresis in Association and Dissociation of Poly(N-isopropylacrylamide) Chains in Water.* Macromolecules, 2006. **39**(6): p. 2325-2329.

38. Lifshitz, I.M. and V.V. Slyozov, *The kinetics of precipitation from supersaturated solid solutions.* Journal of Physics and Chemistry of Solids, 1961. **19**(1-2): p. 35-50.

39. Wagner, C., *Theorie der Alterung von Niederschlägen durch Umlösen (Ostwald-Reifung).* Zeitschrift für Elektrochemie, 1961. **65**(7-8): p. 581-591.